Ordered Zinc Antimonate Nanoisland Attachment and Morphology Control of ZnO Nanobelts by Sb Doping

Baochang Cheng,*,† Baixiang Tian,† Wei Sun,† Yanhe Xiao,† Shuijin Lei,† and Zhanguo Wang‡

Institute for Advanced Studying and School of Materials Science and Engineering, Nanchang University, Nanchang 330031, P. R. China, and Key Laboratory of Semiconductor Materials Science, Institute of Semiconductors, Chinese Academy of Sciences, Beijing 100083, P. R. China

Hierarchical heterostructures of zinc antimonate nanoislands on ZnO nanobelts were prepared by simple annealing of the polymeric precursor. Sb can promote the growth of ZnO nanobelts along the [552] direction because of the segregation of Sb dopants on the $+(001)$ and (110) surfaces of ZnO nanobelts. Furthermore, the ordered nanoislands of toothlike $ZnSb_2O_6$ along the $[001]_{ZnO}$ direction and rodlike $Zn_7Sb_2O_{12}$ along the $[110]_{ZnO}$ direction can be formed because of the match relation of the lattice and polar charges between ZnO and zinc antimonate. The incorporation of Sb in a ZnO lattice induces composition fluctuation, and the growth of zinc antimonate nanoislands on nanobelt sides induces interface fluctuation, resulting in dominance of the bound exciton transition in the room temperature near-band-edge (NBE) emission at relatively low excitation intensity. At high excitation intensity, however, Auger recombination makes photogenerated electrons release phonon and relax from the conduction band to the trap states, causing the NBE emission to gradually saturate and redshift with increasing excitation intensity. The green emission more reasonably originates from the recombination of electrons in shallow traps with doubly charged V_O^{**} oxygen vacancies. Because a V_O^{**} center can trap a photoactivated electron and change to a singly charged oxygen vacancy V_O^{*} state, its emission intensity exhibits a maximum with increasing excitation intensity.

1. Introduction

ZnO is a wide band gap semiconductor with high exciton binding energy (60 meV), so there is intense interest in studying its optical properties. It has been widely used for fabricating nanolasers, field effect transistors, gas sensors, nanocantilevers, and nanoresonators.[1] However, the properties of pure ZnO are unstable and cannot meet the increasing needs of present applications. To enhance the multifunctionality and applications of ZnO in different fields, it requires different structures and orientations. Therefore, it is necessary to control the growth and modulate the properties of ZnO nanostructures.[2] Because of the three fastest growth directions, $\langle 0001 \rangle$, $\langle 01\bar{1}0 \rangle$, and $\langle 2\bar{1}\bar{1}0 \rangle$, as well as the (0001) polar surfaces induced phenomenon, ZnO nanowires generally refer to a structure elongated in the [0001] direction (namely, *c* axial) with a quasihexagonal cross section, in accordance with the growth habit of wurtzite ZnO crystals. However, nanobelts mainly refer to a growth elongated in the [11$\bar{2}$0] (*a* axial) or [01$\bar{1}$0] (*m* axial) directions with rectangular cross sections.[3] When impurities are mixed into the source material during the vapor-liquid-solid (VLS) growth, more complex ZnO structures can be developed, depending significantly on the temperature and amount of impurities used.[4]

It has been recently demonstrated that electrical, optical, and magnetic properties of ZnO nanostructures can be drastically modified by impurity doping. For example, when ZnO is doped with group III elements such as Al, Ga, and In, it is expected that the dopants act as singly charged donors by substituting Zn. The excess carriers supplied by the impurities to the conduction band contribute to increase the electrical conductivity of ZnO.[5] At a low doping level, composition fluctuation can cause the localization of exciton in energy and momentum spaces, where they are restrained from encountering nonradiative centers; thus, the enhancement of emission efficiency is expected. Furthermore, momentum conservation is lifted because of the disordered potentials.[6] In highly doped or highly excited systems, however, single doping often results in the quenching of photoluminescence (PL) because of the efficient Auger interaction between photoexcited electron–hole pairs and carriers supplied by the doping. When trivalent rare earth Dy^{3+} and group I Li^{+} impurities are doped simultaneously, the band edge emission can be enhanced efficiently because of the compensation of carriers in nanostructures.[7] When Sb is introduced to ZnO, it has higher resistance and diffuse reflectivity than those of the undoped ZnO.[4a,8] Moreover, the introduction of Sb can also alter the morphology of the ZnO nanomaterials, including crystal size, orientation, and aspect ratio, which also have important effects on their electrical and optical properties, gas sensitivity and catalytic properties.[8,9] Limpijumnong et al.[10] have proposed recently a new doping mechanism for As and Sb impurities in ZnO based on a first-principles calculation. It was predicted that group V element As (Sb) could introduce shallow acceptor levels in ZnO, assuming that an Sb atom would substitute for a Zn atom and simultaneously produce two corresponding Zn vacancies. Thus, Sb-doped ZnO shows a strong p-type conduction.[11] It is also reported that antimony spinel helps in attaining better stability at higher voltages of ZnO varistors because of the preferential segregation at grain boundaries leading to the formation of separate spinel grains.[12] In this study, Sb-doped ZnO is prepared by simple annealing of the polymetic precursor. It is expected that the morphology

* To whom correspondence should be addressed. E-mail: bcheng@ vip.sina.com. Fax: +86-791-3969554.
† Nanchang University.
‡ Chinese Academy of Sciences.

Zinc Antimonate Nanoisland Attachment

J. Phys. Chem. C, Vol. 113, No. 22, 2009 **9639**

of the nanostructure can be controlled, and its properties can be improved.

2. Experimental Section

Hierarchical nanostructures were synthesized by the in situ chemical vapor reaction method described in our previous work.[4b,7] All reagents are of analytical grade. $SbCl_3$ and $Zn(NO_3)_2$, with a ratio 5%, were dissolved in deionized water, and then appropriate amounts of citric acid and ethylene glycol were added to give a transparent solution. This solution was stirred for 1 h, formed a sol at 80 °C, and subsequently polymerized to a gel at 150 °C for 10 h. The solid resin was prepyrolyzed at 400 °C to form an amorphous composite precursor. The resulting amorphous precursor mixture was then ground, transferred to a ceramic crucible covered with a ceramic lid, and put into a box furnace. The system was then heated to a nominal furnace temperature of 900 °C and kept at this temperature for 120 min. After the furnace had cooled to room temperature, large amounts of a cottonlike product were obtained from the crucible.

The morphology and structure of the as-synthesized products were studied by means of X-ray diffraction (XRD, Phillips X'Pert PRO with Cu Kα radiation), field emission scanning electron microscopy (FESEM, FEI Siron 200), transmission electron microscopy (TEM, JEOL JEM-2000FX) equipped with energy dispersive X-ray spectroscopy (EDS), and high-resolution TEM (HRTEM, JEOL JEM-2010, at 200 kV). The micropho-toluminescence (PL) measurement was performed by a micro-system of a confocal laser micro-Raman spectrometer (LABRAM-HR, France Jobin-Yvon Company) at room temperature, which was conducted in a backscattering geometry using the 514.5 nm line of an Ar^+ laser and the 325 nm line of a He−Cd laser as the excitation light sources. The output power of the laser is about 2 mW, and the incident light is focused on a spot about 5 μm in diameter by a microscopic objective. The signals were collected in a backscattering configuration. For the low-temperature PL measurement, the sample was placed in a liquid nitrogen cryostat using the 325 nm line of a Kimmon He−Cd laser as the excitation resource. A lock-in amplifier was used to filter the PL signal related to the modulated laser.

3. Results and Discussion

3.1. Morphology and Growth Mechanism. Representative XRD patterns for the sample are shown in Figure 1. As evident from the XRD analysis, the samples are mainly composed of a hexagonal wurtzite-structured ZnO phase. In addition, some weak diffraction peaks of a tetragonal ordonezite-structured $ZnSb_2O_6$ (JPCDS NO.38−0453) and a cubic reverse spinel-structured $Zn_7Sb_2O_{12}$ (JPCDS NO.15−0687) are also observed. From the measured (002) and (110) ZnO diffraction peaks of the X-ray diffraction spectra, the lattice constant is estimated to be $c = 0.51746$ nm and $a = 0.32410$ nm. Compared with those of the pure ZnO nanostructures ($c = 0.52066$ and $a = 0.32496$ nm),[4b] the lattice takes place at contraction due to the substitution of smaller ionic radium Sb^{5+} (0.065 nm) for Zn^{2+} (0.074 nm).

The as-synthesized sample was analyzed by FESEM to demonstrate the high yield and structural control. The result given in Figure 2a shows a typical growth of a beltlike structure. From the enlarged FESEM image (Figure 2b−d), it can be seen that the ribbon is a thin crystal slab with nanoislands on the two sides, and furthermore, the morphology and spread direction of the islands are different on the two sides. It is also noticed that these islands are not grown randomly around the nanobelts
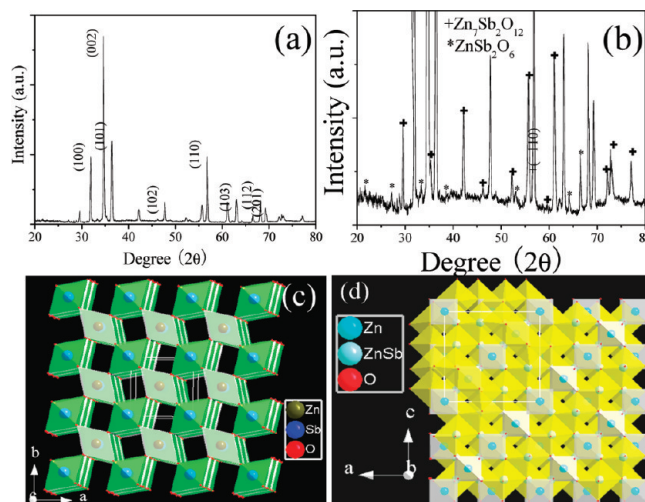
Figure 1. (a) XRD pattern of the as-synthesized sample. (b) Enlarged pattern $Zn_7Sb_2O_{12}$ and $ZnSb_2O_6$ phases are marked by + and *, respectively. (c) and (d) Three dimensional sketch of tetragonal trirutile-type $ZnSb_2O_6$ and cubic reverse spinel-type $Zn_7Sb_2O_{12}$.
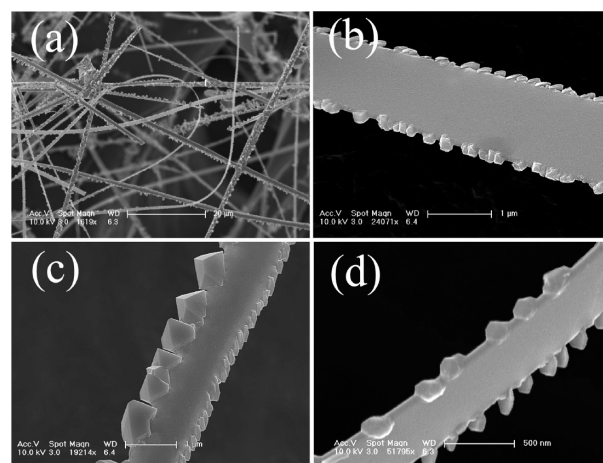

Figure 2. (a) FESEM image of the product. (b), (c), and (d) Enlarged images showing hierarchical nanostructures.

but appear to be aligned along special directions of the nanobelts in some order.

The hierarchical nanostructure was further determined by TEM and selected area electron diffraction (SAED). The SAED analysis, taken with the incident beam perpendicular to the surface of the nanobelt center and inset in Figure 3a and indexed to be [$\bar{1}$10] ZnO, shows that the growth front of the nanobelt is ±(112) and the top/bottom surface is ±(110). Because the normal direction of the (112) plane is [110.389] ≈ [552], the growth direction of nanobelts perpendicular to the (112) planes is [552]. Additionally, the TEM image of the nanostructure exhibited in Figure 3a clearly displays the anisotropic distribu-tion of double-sided island arrays. On one side are relatively large toothlike islands, extending along the [001] direction, and on the other side are relatively small rodlike islands, extending along the [110] direction. The direction of the nanobelt is marked in Figure 3a. A HRTEM image, taken from the edge region of nanobelts without surface nanoislands, shows that the clear lattice fringes correspond to the (002) facets of ZnO. Energy dispersive X-ray spectroscopy (EDS) compositional analyses, taken in various regions, were performed in situ in TEM to investigate Zn and Sb distribution. As shown in Figure 3, besides the Cu and C peaks from the carbon-coated TEM grid, Zn, Sb, and O peaks are present in the spectrum from the island on the
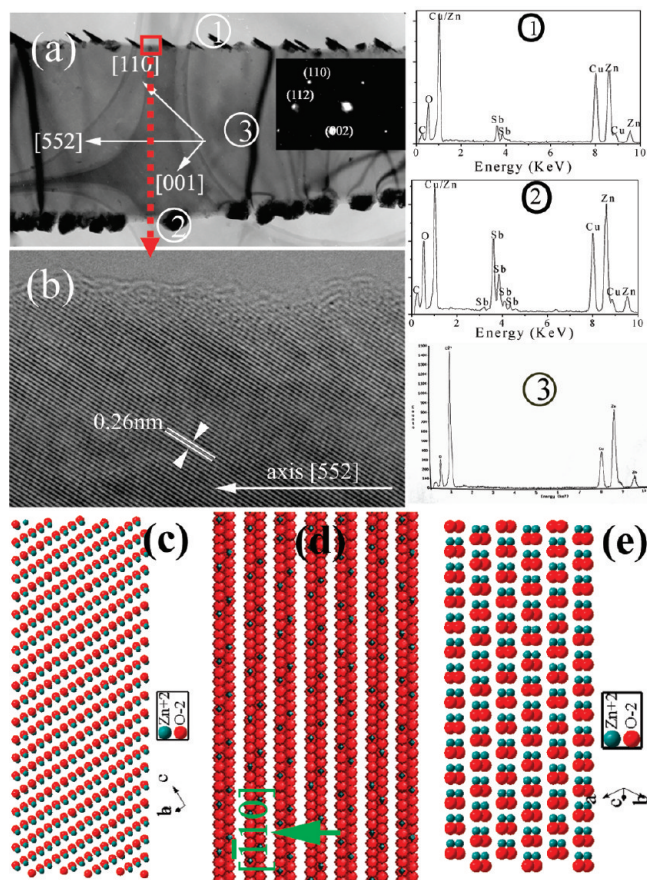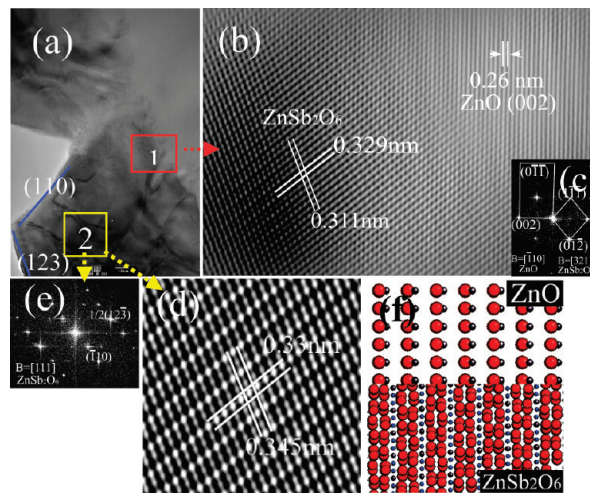
Figure 3. (a) TEM brightfield image and corresponding SAED pattern (inset) taken from the center region of the nanobelt. (b) HRTEM image of the region marked with the red □ in panel a. (c), (d), and (e) Schematic model for the atomic arrangements of ZnO nanobelts projected along [$\bar{1}$10] (top), [552] (cross section), and [1$\bar{1}$1] (side) direction, respectively. EDS spectra in (1), (2), and (3) are taken from the corresponding regions in panel a.

Figure 4. (a) Low-magnification HRTEM image from the nanobelt edge with toothlike islands. (b) Lattice image and corresponding FFT analysis pattern (c) from red □ region 1. (d) Lattice image and corresponding FFT analysis pattern (e) from yellow □ region 2. (f) Schematic model for the atomic arrangements of ZnO (upper) and $ZnSb_2O_6$ (lower) projected along the [$\bar{1}$10] and [321] directions, respectively, displaying the alternating arrangement of positively and negatively charged atoms for the epitaxial planes of $(001)_{ZnO}$ and $(103)_{ZnSb_2O_6}$.

Figure 5. (a) and (b) HRTEM images and corresponding SAED pattern (lower left inset in panel b) from a $ZnSb_2O_6$ toothlike island, taken from the [111] zone axis, showing a superstructure characteristic. The lower right inset in panel b of the corresponding structure model (3 × 3 × 3) of $ZnSb_2O_6$ projected along [111] is superimposed.
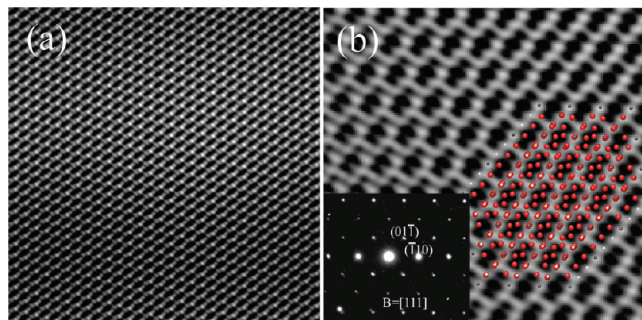
two sides. The content of Sb in the central region of the nanobelt rod is hardly detected because of a relatively low concentration and limited instrument resolution, indicating that the nanobelt is mainly composed of ZnO. It is worth noting that the concentration ratio of Zn to Sb in the two side islands of the nanobelts is different, about 1:2 and 7:2 in toothlike and rodlike districts, respectively.

HRTEM images, including the belt and bilateral nanoislands, are given in Figures 4 and 5, respectively. The fast Fourier transformation (FFT) analysis (Figure 4c), taken in red □ region 1 from the interface between relative large toothlike islands and a nanobelt, shows a superposition of two sets of single-crystal diffraction spots, which are indexed to be [$\bar{1}$10] ZnO and [321] $ZnSb_2O_6$, with an epitaxial orientation. The HRTEM image (Figure 4b) further shows the toothlike island is $ZnSb_2O_6$, and the nanobelt is ZnO with the epitaxial relationships $(001)_{ZnO} \parallel (10\bar{3})_{ZnSb_2O_6}$ and $[\bar{1}10]_{ZnO} \parallel [321]_{ZnSb_2O_6}$. Furthermore, $ZnSb_2O_6$ grows along the ZnO [001] direction on the side surface of the ZnO nanobelt. The lattice image in yellow □ region 2 and the corresponding FFT analysis, which is far from the interface, show that the zone axis becomes a [111] direction.

Figure 5 shows the HRTEM images of a relatively large $ZnSb_2O_6$ toothlike island and the corresponding SAED pattern taken from the [111] zone axis. Besides the main reflections of the substructure, weaker diffraction maxima located at $(0k\bar{l})$ ($k + l = 3n$, n is an integer) can be observed, indicating a formation of a superlattice in the $(04\bar{1})$ direction [about the

normal direction of the $(01\bar{1})$ plane]; the corresponding structure model, projected along [111], is superimposed in the HRTEM image as well.

The SAED pattern (inset in Figure 6a), taken in the region between the relative narrow rodlike island and nanobelt, shows a superposition of two sets of single-crystal diffraction spots, which are indexed to be [$\bar{1}$10] ZnO and [$\bar{1}\bar{1}$2] $Zn_7Sb_2O_{12}$, with the epitaxial relation $(002)_{ZnO} \parallel (111)_{Zn_7Sb_2O_{12}}$, $(110)_{ZnO} \parallel (2\bar{2}0)_{Zn_7Sb_2O_{12}}$, and $[\bar{1}10]_{ZnO} \parallel [\bar{1}\bar{1}2]_{Zn_7Sb_2O_{12}}$. From the HRTEM image in Figure 6b, some moire fringes can be clearly seen on the islands, indicating a slight difference in the lattice constants between the ZnO nanobelt and $Zn_7Sb_2O_{12}$ islands and the growth of $Zn_7Sb_2O_{12}$ epitaxially on the surface of (002) ZnO.

Zinc diantimonate ($ZnSb_2O_6$) exhibits semiconducting properties with a band gap of 3.5 eV.[13] It crystallizes as a trirutile-type structure that contains three rutile units stacked along the c axis as shown in Figure 1c. The Zn and Sb atoms are octahedrally coordinated by six O atoms in each rutile unit, and the octahedrons run parallel to the c axis sharing an edge. The trirutile structure adopts the same space group symmetry as rutile ($P42/mnm$), but the c axis of the unit cell is tripled from the Zn−Sb−Sb−Zn−Sb−Sb− cation sequence observed within

Zinc Antimonate Nanoisland Attachment

*J. Phys. Chem. C, Vol. 113, No. 22, 2009* **9641**
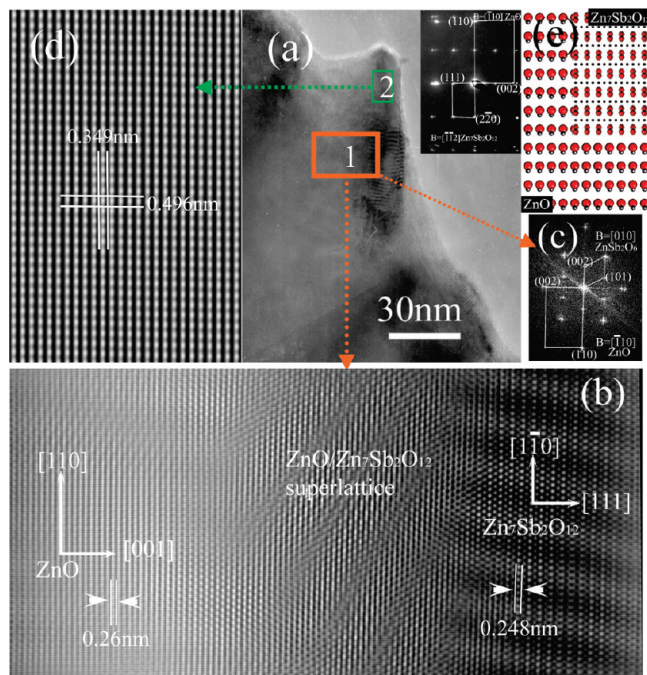
Figure 6. (a) Low-magnification HRTEM image and corresponding SAED pattern from the nanobelt edge with a relatively small rodlike island. (b) Lattice image and corresponding FFT analysis pattern (c) from red □ region 1. (d) Lattice image from green □ region 2. (e) Schematic model for the atomic arrangements of the epitaxial planes, $(002)_{ZnO} \parallel (111)_{Zn_7Sb_2O_{12}}$, and $(110)_{ZnO} \parallel (2\bar{2}0)_{Zn_7Sb_2O_{12}}$.

each rutile chain.[14] Therefore, $ZnSb_2O_6$ presents a superstructure along the normal direction of a $(01\bar{1})$ plane, verified by the HRTEM image and corresponding SAED pattern (Figure 5). $Zn_7Sb_2O_{12}$ is known to crystallize in the inverse spinel structure. In this structure, 2/3 of Zn^{2+} cations are located on tetrahedral sites, and the remaining 1/3 of Zn^{2+} cations and all Sb^{5+} cations are located in octahedral positions.[15]

The anisotropic growth of toothlike $ZnSb_2O_6$ along the [001] direction and rodlike $Zn_7Sb_2O_{12}$ along the [110] direction on the two different sides of ZnO nanobelts results from the surface polarity of ZnO and the match relation of lattice and polar charges between ZnO and zinc antimonate. Structurally, the wurtzite ZnO crystal is described as a number of alternating planes composed of 4-fold tetrahedral-coordinated O^{2-} and Zn^{2+} ions, stacked alternatively along the *c* axis (Figures 3c and 4f). The (001) and $(00\bar{1})$ surfaces are terminated with Zn and O, respectively, resulting in positively and negatively charged polar surfaces.[16] As the dopants are introduced in the nanosized matrices, on the one hand, partial solutes can cause Langmuir adsorption at the single-crystal nanobelt surfaces due to the difference in the adsorption enthalpy between dopants at a grain boundary site and at a lattice site, and on the other hand, due to the difference in the ionic radius between Zn^{2+} and Sb^{5+}, it is likely that substitution of dopants for zinc in the lattice results in a misfit strain energy, which contributes to the driving force for segregation.[17] Furthermore, as the size reduces to nanometer scales, the nanostructures possess relatively high specific surface energy due to the large surface-to-volume ratios. Thus, the solutes prefer to segregate from the nanostructured host and occupy the surface of the nanostructures, which contributes toward a decreased surface energy or reduced surface mobility.[18] Because of nonactivity in the $[00\bar{1}]$ direction, Sb tends to preferentially segregate on the Zn^{2+}-terminated active (001) surface rather than O^{2-}-terminated $(00\bar{1})$ inert surface. The surface energy of (001) planes is reduced, crystal growth along

the $\pm(001)$ orientation is suppressed, and then the morphology of the ZnO nanostructures can be controlled. ZnO nanobelts generally grow along the $[01\bar{1}0]$ or $[0001]$ directions and furthermore form at relatively low temperature. It is due to an enormous decrease in the surface energy of ZnO and a passivation for the (001) facet of ZnO that the ZnO nanobelt is formed anisotropically along the [552] direction, and its top/ bottom surface is $\pm(110)$. The nonuniform distribution of the impurities at the surface layers of the nanostructures easily leads to a local lattice disorder and the formation of microprotuberances (active regions), which are locally enhanced electric fields created by charge concentrations.[19] As a consequence, the microprotuberances can serve as new crystal nucleus dots, and subsequently, the nanoisland arrays sprout and grow on the two different sides of ZnO nanobelts, which will reduce the charge accumulation due to the electric field fluctuations at the growing tip and branch arrays resulting from electrostatic repulsion. In the region between relatively large toothlike islands and ZnO nanobelts, although the plane spacing of $(002)_{ZnO}$ (0.26033 nm) and $(103)_{ZnSb_2O_6}$ (0.2569 nm) is similar (mismatch of 0.25%), there is no proper plane in $ZnSb_2O_6$ to match with the $(100)_{ZnO}$ planes. Therefore, the zone axis vertical to the surface of $ZnSb_2O_6$ toothlike islands away from the interface becomes [111] to reduce the stress, and the corresponding HRTEM image and FTT analysis are shown in panels d and e of Figure 4. In the region between the relatively narrow rodlike islands and ZnO nanobelt, the lattice mismatch is 4.94% between $(002)_{ZnO}$ (0.26033 nm) and $(222)_{Zn_7Sb_2O_{12}}$ (0.24808 nm), and 6.94% between $(110)_{ZnO}$ (0.16247 nm) and $(440)_{Zn_7Sb_2O_{12}}$ (0.15192 nm). As seen from the projected images of the $ZnSb_2O_6$, $Zn_7Sb_2O_{12}$, and ZnO structure models in Figures 4f and 6e, the positive and negative charges exhibit an alternative stacking along the (103) surface of $Zn_2Sb_2O_6$, (111) surface of $Zn_7Sb_2O_{12}$, and (100) surface of ZnO. The match relation of lattice and polar charges results in the growth of toothlike $Zn_2Sb_2O_6$ along the [001] direction and rodlike $Zn_7Sb_2O_{12}$ along the [110] direction on the different sides of the ZnO nanobelts. Considering the crystal structures, we initiated uncatalyzed surface growth of zinc antimonate around the particular outer surface of the ZnO nanobelts. A coherent wetting layer was formed, making it impossible to have long distance epitaxial growth of zinc antimonate on ZnO, which tend to form textured islands on the special surface of ZnO using the Stranski−Krastanow (S−K) mechanism due to the inexact lattice match. Because of different chemical activity between (001) and (110) facets, the Sb segregates more readily on the (001) surface. Thus, the volume of toothlike $ZnSb_2O_6$ islands is larger than that of rodlike $Zn_7Sb_2O_{12}$ islands.

3.2. Photoluminescence Properties. The excitation power-dependent photoluminescence (PL) was measured at room temperature using the 325 nm line of a He−Cd laser as an excitation source, and the results are shown in Figure 7. Excitation light ranges in intensity between about 0.2 and 20 kW/cm^2. As can be seen from the PL spectra (Figure 7a), the sample exhibits a narrow UV emission related to the near-band-edge (NBE) emission and a broad green emission band related to deep level defects. The NBE emission shows a significant redshift from 383 to 398 nm, with increasing excitation power intensity from 0.2 to 20 kw/cm^2 (Figure 7b). Spectrally integrated PL intensities are plotted as a function of excitation laser intensity in Figure 7c. In a low excitation region below 0.25 I_0, the PL intensity grows almost linearly with excitation intensity (as indicated by the dotted line). Conversely, in the higher excitation intensity region (>0.25 I_0), the saturation of
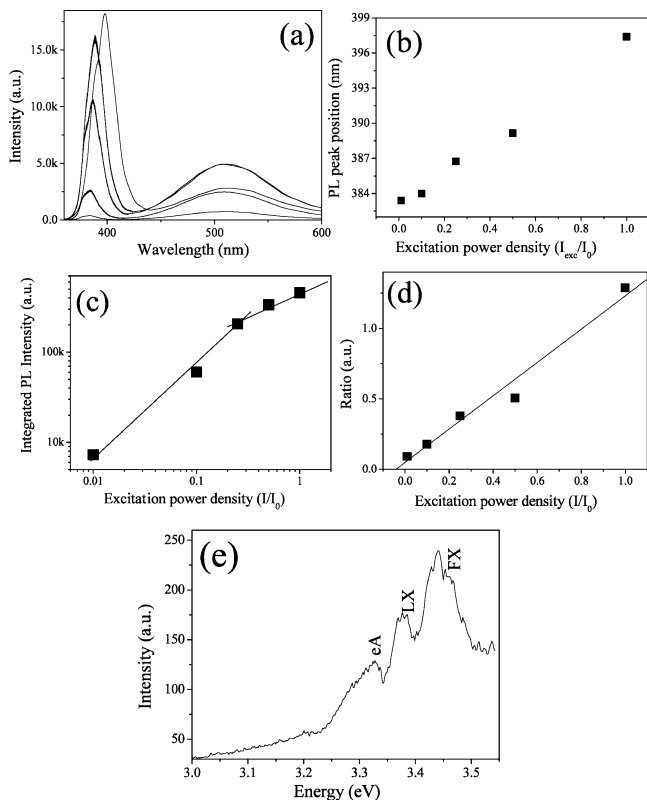
Figure 7. (a) Excitation power intensity-dependent PL of the nanostructures measured at room temperature, where I_0 is about 20 kW/cm^2. Position (b) and integrated intensity (c) of the band edge PL peaks. (d) Integrated intensity ratio of the band edge PL emission to the green emission versus the excitation power intensity. Solid ■ represent experimental data, and the curves represent corresponding fits. (e) Band edge PL spectra measured at 77 K.

the PL intensity is clearly apparent. For the green emission, its intensity increases initially (to 0.25 I_0) and then decreases with increase in excitation intensity, while its position is hardly affected and remains at 515 nm. With increasing excitation fluence, the UV emission band in integrated intensity relative to the green emission band (Figure 7d) almost increases linearly and finally dominates the spectrum.

In elucidating the nature of luminescence from semiconductors, the excitation intensity dependence of the PL spectra is an important consideration. The behavior of the luminescence intensity versus the excitation power intensity can be used to characterize the exciton, donor−acceptor pair, and free-to-boundlike transitions. On the basis of the radiative recombination rate model, it has been established that the luminescence integrated intensity I_{PL} can be expressed as $I_{PL} = \eta I^{\alpha}_{laser}$.[20] In this relation, I_{laser} is the excitation power intensity, η is the emission efficiency, and the exponent α represents the radiative recombination mechanism. For excitonic recombination, $1 < \alpha < 2$; for band gap emission, i.e., electron−hole bimolecular recombination $\alpha \sim 2$; and $\alpha < 1$, when an impurity is involved in the transitions as well as for free-to-bound and donor−acceptor pair transitions. The NBE emission as a function of the excitation intensity is plotted, and the results are shown in Figure 7c. At excitation power intensity below 0.25 I_0, α is about 1.2, while α is decreased to about 0.8 at excitation power intensity above approximately 0.25 I_0. This indicates that the emission originates from the excitonic recombination at low excitation intensity and the emission mechanism changes with increasing excitation intensity. The incorporation of Sb in a ZnO lattice can cause composition fluctuation and, furthermore, the growth of zinc

Antimonate nanoislands on ZnO nanobelts can cause interface fluctuation, which results into the localization of excitons and the emergence of the tail state. Because excitons become localized in energy and momentum spaces in the disordered potentials, they are restrained from encountering nonradiative centers, and thus, the enhancement of emission efficiency is expected.[8] Therefore, at low excitation densities, PL is completely dominated by the bound exciton emission. With increasing excitation intensity, more than one excitons per nanostructure are created. When the number of excitons created per nanostructure is so large that the ratio of the nanostructural volume to the number of excitons is smaller than the exciton volume, a Mott-like transition to the electron−hole plasma can be expected. The presence of disorders and surface heterostructures in the nanobelts would give rise to the trap states below the conduction band edge and above the valence band edge. In high-intensity carrier plasma, the photogenerated electrons can release phonons and relax from the conduction band to the trapped states and reach the local potential minima. Thus, Auger recombination, which is a three-carrier interaction, where an electron−hole (e−h) pair transfers its energy nonradiatively to a third nearby carrier, emerges and dominates gradually with increasing excitation intensity. Consequently, the PL intensity−excitation dependence should be sublinear at high excitation intensity, and the exponent α is decreased to less than 1.[21] Furthermore, the rate of the Auger recombination is proportional to the third power of the carrier intensity.[22] Thus, the NBE emission will saturate with further increasing excitation intensity. Additionally, once the radiative transition occurs from these trap states, a steady redshift in the emission spectra would occur. The spectral redshift and broadening on the low-energy side suggest that the many body effect, involving localized excitons, may play a significant role under the high excitation condition.[23]

The origin of the green emission is still under debate.[24] A number of different hypotheses have been proposed to explain the green emission such as a transition between a singly ionized oxygen vacancy V_O^* and photoexcited hole, a transition between an electron close to the conduction band and a deeply trapped hole at V_O^{**}, surface defects, etc.[25] Oxygen vacancies in ZnO can occur in three different charge states: neutral V_O, singly charged V_O^*, and doubly charged V_O^{**}. The singly charged V_O^* is generated by the nonradiative recombination of the neutral V_O with holes from shallow traps near the valence, and the doubly charged V_O^{**} is created by the nonradiative recombination of shallow trap holes with the deep trap V_O^*. The intensity of V_O^{**} is inversely proportional to the square root of the free carrier concentration in ZnO particles.[25a] Under illumination, these V_O^{**} centers can trap a photoactivated electron and change to V_O^* states. Furthermore, more free carriers can freezeout at a higher excitation power intensity. Consequently, the V_O^{**} concentration increases initially and then decreases with increasing excitation power intensity, and the green emission should come from the recombination of electrons in shallow traps close to conduction band edge with deeply trapped holes at V_O^{**} centers. It is generally agreed that following band excitation the photogenerated electrons and holes are captured by shallow traps on time scales faster than the exciton lifetime.[25c] At higher excitation intensity, electrons relax from the conduction band to shallow trap states and then directly return to shallow acceptor levels because of the decrease of V_O^{**} concentration. Thus, the PL integrated intensity ratios of the UV emission to the deep level green emission increase with an increase in excitation intensity.

Low-temperature measurement is performed at 77 K for further study of the optical properties and is shown in Figure

7e. Three emission lines appear around NBE, centering at 3.44, 3.37, and 3.32 eV. The dominant peak at 3.44 eV is ascribed to the free exciton (FX) emissions. The peak located near 3.37 eV can be attributed to a localized exciton (LE) bound by impurity, emissions in bulk-type ZnO, and the peak near 3.32 eV is assigned to the free electron-to-acceptor (eA) transition.

4. Conclusions

Hierarchical heterostructures of zinc antimonate nanoislands on the two sides of ZnO nanobelts were prepared by a simple annealing of the polymeric precursor. ZnO nanobelts grow along the [552] direction, and the top/bottom surface is $\pm(\bar{1}10)$, indicating that the shape of the ZnO nanomaterials could be controlled via Sb doping. The polar charge alignment of ZnO makes Sb preferentially segregated on specific surfaces [+(001) and (110)] of ZnO nanobelts, resulting in the formation of relatively ordered zinc antimonate nanoisland arrays based on the S−K mechanism due to the lattice misfit. Furthermore, the match relation of lattice and polar charges between ZnO and zinc antimonate results in the formation of toothlike $ZnSb_2O_6$ along the $[001]_{ZnO}$ direction and rodlike $Zn_7Sb_2O_{12}$ along the $[110]_{ZnO}$ direction on two different sides of ZnO nanobelts. The incorporation of Sb in a ZnO lattice induces composition fluctuation, and growth of zinc antimonate nanoislands on ZnO nanobelts induces interface fluctuation. As a result, at low excitation power intensity the room temperature near-band-edge (NBE) emission is dominated by the bound exciton transition. At high excitation intensity, however, Auger recombination makes photogenerated electrons release phonon and relax from the conduction band to the trap states, causing the NBE emission to gradually saturate and redshift with increasing excitation intensity. The green emission should be more reasonably attributed to the recombination of electrons in shallow traps with doubly charged V_O^{**} vacancies. Because the V_O^{**} centers can trap a photoactivated electron and change to a V_O^* state, its emission intensity exhibits a maximum with increasing excitation intensity, and furthermore, the integrated intensity ratio of the UV emission band to the green emission band almost increases linearly.

References and Notes

(1) (a) Huang, M. H.; Mao, S.; Feick, H.; Yan, H.; Wu, Y.; Kind, H.; Weber, E.; Russo, R.; Yang, P. *Science* **2001**, *292*, 1897. (b) Hughes, W. L.; Wang, Z. L. *Appl. Phys. Lett.* **2003**, *82*, 2886. (c) Bai, X. D.; Wang, E. G.; Bai, P. X.; Wang, Z. L. *Appl. Phys. Lett.* **2003**, *82*, 4806. (d) Zhang, Y.; Xu, J. Q.; Xiang, Q.; Li, H.; Pan, Q. Y.; Xu, P. C. *J. Phys. Chem. C* **2009**, *113*, 3430.

(2) (a) Özgür, Ü.; Alivov, Ya. I.; Liu, C.; Teke, A.; Reshchikov, M. A.; Doğan, S.; Avrutin, V.; Cho, S. J.; Morkoç, H. *J. Appl. Phys.* **2005**, *98*, 041301. (b) Heo, Y. W.; Norton, D. P.; Tien, L. C.; Kwon, Y.; Kang, B. S.; Ren, F.; Pearton, S. J.; LaRoche, J. R. *Mater. Sci. Eng. R* **2004**, *47*, 1. (c) Cheng, B. C.; Yu, X. M.; Liu, H. J.; Wang, Z. G. *J. Phys. Chem. C* **2008**, *112*, 16312. (d) Li, J. Y.; Zhang, Q.; Peng, H. Y.; Everitt, H. O.; Qin, L. C.; Liu, J. *J. Phys. Chem. C* **2009**, *113*, 3950. (e) Hao, Y. F.; Meng, G. W.; Wang, Z. L.; Ye, C. H.; Zhang, L. D. *Nano Lett.* **2006**, *6*, 1650. (f) Yan, X. Q.; Gu, Y. S.; Zhang, X. M.; Huang, Y. H.; Qi, J. J.; Zhang, Y.; Fujita, T.; Chen, M. W. *J. Phys. Chem. C* **2009**, *113*, 1164. (g) Hao, Y. F.; Meng, G. W.; Ye, C. H.; Zhang, L. D. *Appl. Phys. Lett.* **2005**, *87*, 033106.

(3) (a) Pan, Z. W.; Dai, Z. R.; Wang, Z. L. *Science* **2001**, *291*, 1947. (b) Kong, X. Y.; Wang, Z. L. *Nano Lett.* **2003**, *3*, 1625.

(4) (a) Zou, K.; Qi, X. Y.; Duan, X. F.; Zhou, S. M.; Zhang, X. H. *Appl. Phys. Lett.* **2005**, *86*, 013103. (b) Cheng, B. C.; Xiao, Y. H.; Wu, G. S.; Zhang, L. D. *Adv. Funct. Mater.* **2004**, *4*, 913. (c) Lommens, P.; Loncke, F.; Smet, P. F.; Callens, F.; Poelman, D.; Vrielinck, H.; Hens, Z. *Chem. Mater.* **2007**, *19*, 5576.

(5) (a) Jin, Z. C.; Hamberg, I.; Granqvist, C. G. *J. Appl. Phys.* **1988**, *64*, 5117. (b) Ning, Z. Y.; Cheng, S. H.; Ge, S. B.; Chao, Y.; Gang, Z. Q.; Zhang, Y. X.; Liu, Z. G. *Thin Solid Films* **1997**, *307*, 50.

(6) Yamaguchi, S.; Kurusu, H.; Kawakami, Y.; Fujita, S. *Phys. Rev. B.* **2000**, *61*, 10303.

(7) Cheng, B. C.; Yu, X. M.; Liu, H. J.; Fang, M.; Zhang, L. D. *J. Appl. Phys.* **2009**, *105*, 014311.

(8) (a) Zeng, D. W.; Xie, C. S.; Zhu, B. L.; Song, W. L.; Wang, A. H. *Mater. Sci. Eng., B* **2003**, *104*, 68. (b) Yang, Y.; Qi, J. J.; Liao, Q. L.; Zhang, Y.; Tang, L. D.; Qin, Z. *J. Phys. Chem. C* **2008**, *112*, 17916.

(9) Yang, Y.; Qi, J. J.; Zhang, Y.; Liao, Q. L.; Tang, L. D.; Qin, Z. *Appl. Phys. Lett.* **2008**, *92*, 183117.

(10) Limpijumnong, S.; Zhang, S. B.; Wei, S. H.; Park, C. H. *Phys. Rev. Lett.* **2004**, *92*, 155504.

(11) (a) Xiu, F. X.; Yang, Z.; Malapu, L. J.; Zhao, D. T.; Liu, J. L.; Beyermann, W. P. *Appl. Phys. Lett.* **2005**, *87*, 152101. (b) Malapu, L. J.; Xiu, F. X.; Yang, Z.; Zhao, D. T.; Liu, J. L. *Appl. Phys. Lett.* **2006**, *88*, 112108.

(12) Ezhilvalavan, S.; Kutty, T. R. N. *Appl. Phys. Lett.* **1996**, *68*, 2693.

(13) Mizoguchi, H.; Woodward, P. M. *Chem. Mater.* **2004**, *16*, 5233.

(14) Kikuchi, N.; Hosono, H.; Kawazoe, H. *J. Am. Ceram. Soc.* **2005**, *88*, 2793.

(15) (a) Bayer, G. *Naturwissenschaften* **1961**, *48*, 46. (b) Linares, R. C.; Mills, A. D. *Acta Crystallogr.* **1962**, *15*, 1048.

(16) Wang, Z. L.; Kong, X. Y.; Zuo, J. M. *Phys. Rev. Lett.* **2003**, *91*, 185502.

(17) (a) Lee, J. R.; Chiang, Y. M.; Ceder, G. *Acta. Mater.* **1997**, *45*, 1247. (b) Raola, O. E.; Strouse, G. F. *Nano Lett.* **2002**, *2*, 1443.

(18) (a) Maciela, A. P.; Lisboa-Filhoa, P. N.; Leitea, E. R.; Paiva-Santosb, C. O.; Schreinerc, W. H.; Manietteb, Y.; Longoa, E. *J. Eur. Ceram. Soc.* **2003**, *23*, 707. (b) Bachir, S.; Azuma, K.; Kossanyi, J.; Valat, P.; Ronfard-Haret, J. C. *J. Lumin.* **1997**, *75*, 35.

(19) Fonseca, L. F.; Resto, O.; Solá, F. *Appl. Phys. Lett.* **2005**, *87*, 113111.

(20) (a) Fouquet, J. E.; Siegman, A. E. *Appl. Phys. Lett.* **1985**, *46*, 280. (b) Chen, X. B.; Huso, J.; Morrison, J. L.; Bergman, L. *J. App. Phys.* **2006**, *99*, 046105. (c) Schmidt, T.; Lischka, K.; Zulehner, W. *Phys. Rev. B* **1992**, *45*, 8989.

(21) Babentsov, V.; Sizov, F. *Opto-Electron. Rev.* **2008**, *16*, 208.

(22) Ghanassi, M.; Schanne-Klein, M. C.; Hache, F.; Ekimov, A. L.; Ricard, D.; Flytzanis, C. *Appl. Phys. Lett.* **1993**, *62*, 78.

(23) Han, X. F.; Weng, Y. X.; Pan, A. L.; Zou, B. S.; Zhang, J. Y. *Appl. Phys. Lett.* **2008**, *92*, 032102.

(24) Djurišić, A. B.; Choy, W. C. H.; Roy, V. A. L.; Leung, Y. H.; Kwong, C. Y.; Cheah, K. W.; Gundu Rao, T. K.; Chan, W. K.; Lui, H. F.; Surya, C. *Adv. Funct. Mater.* **2004**, *14*, 856.

(25) (a) Vanheusden, K.; Seager, C. H.; Warren, W. L.; Tallant, D. R.; Voigt, J. A. *Appl. Phys. Lett.* **1996**, *68*, 403. (b) van Dijken, A.; Meulenkamp, E. A.; Vanmaekelbergh, D.; Meijerink, A. *J. Phys. Chem. B* **2000**, *104*, 1715. (c) Rakshit, S.; Vasudevan, S. *J. Phys. Chem. C* **2008**, *112*, 4531.